Published in final edited form as:
NMR Biomed. 2011 July ; 24(6): 569–581. doi:10.1002/nbm.1632.

Hypoxic stress and cancer: Imaging the axis of evil in tumor metastasis

Reut Avni, **Batya Cohen**, and **Michal Neeman**
Department of Biological Regulation, Weizmann Institute, Rehovot 76100 Israel

Abstract

Tumors emerge as a result of sequential acquisition of genetic, epigenetic, and somatic alterations promoting cell proliferation and survival. The maintenance and expansion of tumor cells relies on their ability to adapt to changes in their microenvironment, along with acquisition of the ability to remodel their surroundings. Tumor cells interact with two types of interconnected microenvironments, the metabolic cell autonomous microenvironment and the non-autonomous cellular-molecular microenvironment comprising interactions between tumor cells and the surrounding stroma. Hypoxia is a central player in cancer progression, affecting not only tumor cell autonomous functions such as cell division and invasion, resistance to therapy and genetic instability, but also non-autonomous processes such as angiogenesis, lymphangiogenesis and inflammation, all contributing to metastasis. Closely related microenvironmental stressors, affecting cancer progression include in addition to hypoxia, also elevated interstitial pressure and oxidative stress. Non invasive imaging offers multiple means for monitoring the tumor microenvironment and its consequences, and can thus assist in understanding the biological basis of hypoxia and microenvironmental stress in cancer progression, and in development of strategies for monitoring therapies targeted at stress induced tumor progression.

Keywords

Hypoxia; angiogenesis; glycolysis; metastatsis; oxidative stress; imaging; MRI

Introduction

The sequential changes leading to transformation, known as the hallmarks of cancer involve cell autonomous genetic and metabolic alterations along with non cell-autonomous changes in the interaction of the cells with the surrounding stroma (1). Among the most prominent alteration observed in cancer is the exposure of cells to chronic and acute hypoxia. This exposure to hypoxia affects tumor progression in multiple ways including the induction of angiogenesis and a metabolic switch towards elevated glucose uptake and elevated glycolytic fermentation even in the absence of hypoxia, namely the ‘Warburg effect’ (2,3). The metabolism of cancer cells is frequently significantly altered from that of the surrounding normal tissue (4). In normal cells energy homeostasis is balanced by at least three metabolic pathways including glycolysis, lipogenesis and the tricarboxylic acid (TCA) cycle. In tumors, however, a significant fraction of the cellular energy, even under normoxic conditions, is produced by glycolysis (2,3,5). This metabolic transition was proposed to be selected for in cancers, as it can contribute directly to tumor expansion and metastasis (6).

Full address for correspondence: Michal Neeman Department of Biological Regulation Weizmann Institute, Rehovot 76100 Israel Tel: 972-8-9342487 Fax: 972-8-9346264 michal.neeman@weizmann.ac.il.

Europe PMC Funders Author Manuscripts

Hypoxia in cancer

Oxygen deficiency, or hypoxia, is a central microenvironmental tumor stress that arises as a consequence of the expansion of solid tumors by cancer cell proliferation, which is unmatched by the expansion and maintenance of the vasculature supply (Figure 1 A).

Deficiencies in oxygen transport due to chaotic structure and function of the microvessels nourishing the tumor in addition to reduced oxygen transport capacity of the blood, result in oxygen gradients within the tumor based on the distance from a functional blood vessel (7). Thus, tumor cells surrounding functional blood vessels are generally better oxygenated, whereas the tumor cells distant from the vessel are poorly oxygenated. The irregular blood flow in tumors exposes tumor cells not only to chronic hypoxia, but also to acute hypoxia in regions with intermittent blood flow. Hypoxia was recognized to induce gene instability (8), and also to provide an important selective pressure resulting in increased tumor aggressiveness and resistance to hypoxia induced apoptosis. Hypoxia also protects cells from radiation and chemotherapy. Hypoxia was thus demonstrated in clinical trials to be associated with poor prognosis (9,10). In response to hypoxia, expanding tumor cells induce the expression of key molecular programs that promote cell survival, angiogenesis, tumor spread and apoptosis. Many of these pleiotropic actions are orchestrated by hypoxia-inducible factor (HIF) responsible for both sensing and responding to changes in cellular oxygen.

Methods of non-invasive imaging of Hypoxia

Given the importance of hypoxia in cancer progression and therapy, over the recent years there has been a significant effort towards the development of noninvasive imaging methods to detect and assess tumor hypoxia (11). Such imaging tools could potentially replace the invasive pO_2 measurements using polarographic oxygen electrodes, which are considered the “gold standard” (12). Imaging provides the opportunity to monitor the magnitude and spatial pattern of tumor hypoxia over time during therapy (12). A number of tracers, (eg 2-Nitroimidazoles based probes), which are reduced and retained in hypoxic regions, are applied for imaging hypoxia using PET and SPECT(13). Magnetic resonance-based methods proposed for imaging of oxygen can be broadly categorized into three groups: electron paramagnetic resonance (EPR) oximetry, ^{19}F MRI and blood oxygen level-dependent (BOLD) contrast MRI (Figure 1 B-D; Figure 2).

EPR oximetry

EPR spectroscopy, which detects materials with unpaired electrons, can be used to provide information about the local environment of the free radicals, including the level of oxygen in the vicinity of paramagnetic materials (14). EPR oximetry relies on the fact that EPR spectral line-width (R_2) is sensitive to changes in oxygen concentration (Figure 1 B). Thus, quantitative oximetry can be made by calibration of the line broadening, which is directly proportional to the concentration of oxygen (14). The measurement involves the administration of either particulate or soluble oxygen-sensitive paramagnetic spin probes. The particulates are metabolically inert materials, such as lithium phthalocyanine (LiPc) and india ink, that contain un-paired electrons, distributed over many atoms in crystalline materials. These are considered to be very stable spin probes, with a high sensitivity to oxygen concentrations. An important advantage of the particulates probes is that, once introduced, they allow repeated measurement from the same site for many years (15). Soluble probes are more convenient for imaging purposes since they diffuse in the whole tissue albeit exhibit less sensitivity to oxygen concentrations (15).

Standard EPR spectrometers usually operate at much higher frequencies and lower fields than NMR spectrometers, for example 9.5 GHz for a magnetic field of about 0.34 T (16). One of the limitations for in-vivo applications of EPR oximetry is that it suffers from poor tissue penetration at high fields: at fields of 1GHz the penetration depth is about 1 cm, as a consequence limiting the possibility of studying tumors which are not superficial using EPR oximetry. At lower fields (~240 MHz) the penetration is less of a problem but the signal to noise ratio (SNR) is lower (15). Halpern et al reported in 1994 the measurement of oxygen concentration using EPR oximetry in-vivo. Murine fibrosarcomas implanted in the mouse leg were measured at low frequency of 250 MHz after the injection of the oxygen-sensitive spin probe mHCTPO (17). Since then, EPR oximetry has been engaged as a useful tool to measure pO_2 physiological concentrations in various tissues. EPR oximetry studies over the recent years include the development and testing of new paramagnetic spin probes (16,18), pO_2 measurements in tumors (12,15-17,19), comparison to other methods (20), and monitoring dynamic changes of oxygen in tumors by modifying the inhaled gases (12,15,16,19,21) or by pharmacological interventions (22). Thus, the majority of the efforts have concentrated on measuring oxygen tension in tumors, and monitoring pO_2 changes during the course of therapy (12,15,16,19).

The development of high-spatial resolution multisite oximetry technique had further expanded EPR utility by allowing the measurement of pO_2 simultaneously from several sites within the sample (23). Recently, multisite EPR was successfully used to measure changes in oxygen concentration in response to radiation and carbogen breathing in an orthotopic tumor model developed upon inoculation of rat 9L and C6 glioma cell in the rat brain (21). A significant increase in oxygen levels was induced by irradiation and carbogen breathing only in the 9L gliomas, thus emphasizing the tumor-specific effect of irradiation on tumor pO_2 and illustrating EPR capabilities of monitoring pO_2 dynamic changes in tumors at their orthotopic position (21).

EPR offers a great promise for future clinical applications by providing an accurate measurement for tissue pO_2 thus, allowing follow-up of tumor oxygenation following therapy. Currently, EPR oximetry has been applied to study superficial tumors in humans (19,24).

EPR allows monitoring of oxygen concentration but lacks complementary anatomical information. Based on the Overhauser effect as combination of EPR and MRI, it is possible to obtain co-registered anatomy with corresponding oxygen status (25). This method is referred to in the literature as PEDRI (proton electron double resonance imaging) or OMRI (overhauser magnetic resonance imaging) (25,26). A strong EPR pulse is used for saturating the EPR resonance, resulting in dipolar coupling of electrons and protons, thus enhancing the NMR proton signals. The amplification depends on the EPR line-widths of the free radical spin probe, which in turn depends inversely on oxygen concentration in the environment of the species (25,26). Field-cycled spectrometers are being used to allow EPR irradiation at low fields, followed by increase in the field to allow acquiring the proton MRI images with high SNR and resolution. This principle was demonstrated by Krishna *et al.* in 2002, in tumor-bearing mice for simultaneous visualization of oxygenation maps and high-quality morphological images (26).

A recent study by Matsumoto *et al.* reported the application of OMRI methodology to obtain information on oxygen status, together with microvascular permeability (27). Using tumor bearing mice and a soluble spin probe, several OMRI images were collected with different hyper-polarization levels. From the profile of the Overhauser enhancement it was possible to determine the oxygen concentration (Figure 1 B). Regions with high vascular permeability

co-localized with hypoxic regions. This technique demonstrates the ability to explore the connection between permeability and hypoxia (27).

Notably, a similar co-localization of vascular permeability and hypoxia was detected using macromolecular BSA-GdDTPA enhanced MRI and mapping of hypoxia by bioluminescence imaging using a luciferase reporter gene driven by HIF-1 α (28). A followup study demonstrated the correlation between hypoxic regions in orthotopic tumors versus subcutaneous and the association with increased angiogenesis and metastasis (29).

^{19}F NMR Oximetry

^{19}F-based oxygen-sensitive probes rely on the linear correlation between ^{19}F longitudinal relaxation rate, R_1, and oxygen tension, pO_2 (30-32). Perfluoro-carbons (PFCs) are non-toxic hydrophobic liquids, which form emulsions that can be infused intravenously into the blood. These emulsions are capable of dissolving a large amount of molecular oxygen allowing their use as blood substitutes. They are chemically stable with an average life time of around 10h, metabolically inert, and their primary clearance is by macrophages and by the reticuloendothelial system (30). PFCs can be used to study tumor hypoxia since they can penetrate through the leaky vasculature characterizing many tumors. It is possible to perform ^{19}F NMR with PFC combined with ^{1}H MRI for anatomical information, thus achieving a reliable map of oxygen levels together with localization. Tumor pO_2 maps are derived from a calibration curve, performed on PFC emulsions, in-vitro.

The choice of PFC is governed by many factors such as high sensitivity to oxygen concentrations, lack or reduced dependence of temperature and complexity of the NMR spectrum (32). Hexafluorobenzene (HFB) is the most widely used probe because of its many advantages as an oxygen reporter: high sensitivity for oxygen concentrations, single and narrow ^{19}F NMR signal, lack of temperature dependence, low cost, easy storage and availability. It does not form emulsions and can be directly injected into tumors, where it remains for many hours (half-life time ~10h), thus allowing repeated measurements for many hours (32). A new assay, FREDOM (fluorocarbon relaxometry using echoplanar imaging for dynamic oxygen mapping), using HFB as a reporter molecule, allows simultaneous measurement of multiple sites within a tumor. This approach revealed dynamic changes in specific tumor locations as a result of interventions, such as hyperoxic gas breathing (32). Validation studies have shown that oxygen tension levels measured with FREDOM technique are similar to those obtained with the Eppendorf histograph (33), and also showed correlation with NIR studies of oxygen probes (34). FREDOM approach has been applied in a range of tumor models (32,35), and also used to show correlations between pO2 at the time of irradiation and tumor growth delay in Dunning prostate rat tumors using HFB as a reporter molecule (36) (Figure 1 C). Recently, snapshot inversion recovery was applied to improve the temporal resolution for 19F MR oximetry (37).

The major hurdle for clinical application of ^{19}F NMR oximetry is the lack of ^{19}F channels in many clinical scanners, and also sensitivity limitations at low field (1.5T), along with a low fraction of the emulsions taken up by the tumors (31). An analogous approach: PISTOL (proton imaging of siloxanes to map tissue oxygenation levels), was applied for mapping pO_2 in animal models using proton NMR (38,39).

Hexamethyldisiloxane (HMDSO) was identified as an oxygen-sensitive NMR probe. It has similar properties to HFB, a single NMR resonance with a distinct chemical shift well separated from water and fat, minimal toxicity, and R_1 relaxation rate that is highly sensitive to oxygen. PISTOL measurement of pO_2 in Dunning prostate tumors in rats challenged by breathing hyperoxic gas was compared to ^{19}F oximetry using FB (Figure 1 D) (38)

Hypoxia inducible factor (HIF-1)

The ability of cells to sense and respond to changes in the concentration of oxygen can be attributed largely to the hypoxia regulated transcription factor HIF-1. HIF-1 is a heterodimeric factor consisting of an oxygen inducible α subunit (HIF-1α) and a constitutively expressed oxygen independent β subunit (HIF-1β, ARNT) (40). Under normal oxygen tension (21%), HIF1α is remarkably labile (half-life of five minutes) being constitutively expressed and degraded (Figure 2 A). The majority of HIFα degradation is regulated by the hydroxylation of two prolyl residues in the oxygen-dependent degradation domain (ODDD) of the protein by HIF prolyl hydroxylases (PHDs) (41). The hydroxylation of HIF1α causes interaction with the von Hippel-Lindau (VHL) protein, a component of an E3 ubiquitin ligase complex. This interaction results in the covalent attachment of ubiquitin chains to lysine residues on HIF-1α thus, earmarking it for proteasome degradation (42). Under hypoxic environment, this hydroxylation-mediated degradation pathway is blocked, thereby allowing HIF-1α to accumulate and translocate in to the nucleus, where it binds to the constitutively expressed HIF-1β. The HIF-1a–HIF1-β dimer binds to hypoxia-responsive-elements (HREs, 5′-RCGTG-3′) located in numerous transcriptional target genes that are implicated in systemic hypoxia responses, such as angiogenesis and erythropoiesis, and cellular hypoxia responses involving energy metabolism, proliferation, motility and autophagy (43).

HIF-1α is not only controlled by oxygen tension, but can be regulated by other factors such as oncogene activation or loss of tumor suppressors. Thus, HIF-1α accumulates in tumor cells even under normoxic conditions due to activation of oncogenes such as Ras, Src and phosphoinositide 3-kinase (PI3K), or loss of tumor suppressors such as VHL or PTEN (44). The pivotal role of HIF in cancer progression is based on the examination of human cancer biopsy samples and experimental animal models. Immunohistochemical analysis has demonstrated that HIF-1α is overexpressed in a broad range of human malignancies including colon, lung, ovary, prostate, skin (melanoma), and stomach cancers Furthermore, HIF-1α accumulation has been discovered in the majority of breast and colon cancer metastases and has been associated with poor patient survival (45). This notion is further supported by various experiments performed with murine and human cancer cell lines deficient of HIF-1α. HIF-1α deficiency resulted in delayed tumor initiation, decreased angiogenesis and metastasis rate (46,47). Thus, HIF-1α protein levels can be used as a prognosis marker in various cancers as well as a predictive biomarker when designing new treatment regimes.

Imaging the role of HIF-1 using BOLD Contrast MRI

Blood-oxygen-level-dependent (BOLD) effect was first described by Ogawa et al for imaging the blood oxygen level in rat brain (48,49). BOLD images reflect the changes in the amount of oxygen bound to hemoglobin in blood and thus can be used for imaging acute and chronic changes in blood flow and oxygenation in tumors.

Deoxygenated hemoglobin is paramagnetic and its compartmentalization in red blood cells (RBC) creates magnetic susceptibility differences between RBC and plasma thus increasing R2′, a term sensitive to variations in local magnetic susceptibility. The transverse relaxation rate ($R_2 = 1/T_2$) may also increase if the size of the variations is as large as the diffusion path length (50). Overall, R_2^* which is the sum of R_2 and R_2', is increased by deoxyhemoglobin. Thus, it has been proposed that tumor R_2^* measurements may provide a sensitive index to tissue oxygenation (12). The functional dependence of T_2^* on oxygenation in a tissue can be approximated by the following relation (Eq. [1]):

$$\frac{1}{T_2^*}\alpha(1-Y)b \quad [1]$$

Where Y is the fraction of oxygenated blood and b is the fractional blood volume (48). In hypoxic tumors where $0 < Y < 0.2$, the contrast produced by the method is primarily dependent on fractional blood volume. BOLD-MRI has been used to study the role of vascular endothelial growth factor (VEGF) in vessel maturation and the functional status of the vascular bed in poorly oxygenated tumors such as subcutaneous models (51,52) and in xenografts with random orientation of sprouting capillaries (53,54).

Maps of functional vasculature using BOLD-contrast showed reduced vascular function in response to hyperoxia, as detected by BOLD-contrast MRI in HIF-1α deficient tumors (Figure 2 B) (55). This correlated with reduced expression of VEGF and reduced vessel density in the HIF-1α–deficient tumors relative to the wild type (55). HIF-1β deficient tumors showed large heterogeneity in BOLD contrast within each individual tumor, but remarkably no consistent differences between wildtype (WT) and c4 Hif-1 beta deficient tumors (Figure 2 C) (56).

Human Von Hippel-Lindau VHL tumors, in which HIF-1 is constitutively activated, were studied by BOLD contrast MRI, showing significant response to anti-angiogenic treatment with halofuginone (Figure 2 D) (57). The effect of inhibition of HIF-1 in tumor bearing mice was investigated using dynamic contrast enhanced (DCE) and diffusion weighted (DW) MRI, demonstrating a reduction in vascular volume and permeability, followed by decreased tumor cellularity (58).

Metabolic shift in solid tumors

A major intracellular adaptation to severe hypoxia is the transition from oxidative phosphorylation to glycolysis as the principal means of ATP generation. Thus, one of the most important aspects of hypoxic HIF-1 is to compensate for the fact that glycolysis generates twenty fold less ATP per mole of glucose compare to oxidative phosphorylation. To balance ATP consumption HIF increases both glucose transfer and glycolysis rate (Figure 3 A). Initially by transcriptional transactivation, HIF-1 elevates the expression of two abundant glucose transporters GLUT1 and GLUT3. Since these transporters pump glucose from its relatively high blood levels to low intracellular levels, thus increasing their protein level increases the flux of glucose into the hypoxic cell (59). To channel this mass of glucose concentration into glycolysis, HIF-1 increases the amounts of key enzymes involved in this process (60).

This increase in the glycolytic rate is accompanied with mitochondrial oxidative phosphorylation attenuation resulting through transcriptional activation of pyruvate dehydrogenase kinase 1 (PDK1) (61). HIF-1 further decreases mitochondrial activity by stimulating Bcl-2/E1B-19K-interacting protein 3 (BNIP3) expression, which selectively triggers mitochondrial autophagy (62). The transition of tumors to high glycolytic activity can be used for tumor detection and monitoring by non-invasive imaging.

Imaging glucose uptake

The primary method for monitoring glucose uptake by tumors is the detection of the accumulation of 2-^{18}F-fluoro-2-deoxy-D-glucose (FDG) by positron emission tomography (PET). The development of PET/CT (computed tomography) (6,63,64) and the recent development of PET/MR (Figure 3 B) had enabled obtaining both molecular and morphological information at the same time (65).

Europe PMC Funders Author Manuscripts

FDG enters the cells by glucose transporters and then phosphorylated by hexokinase to FDG-6-phosphate. The phosphorylation product does not enter the glycolysis pathway, but remains inside the cells where it accumulates. The increased FDG uptake was found to result from upregluation of glucose transporters, in particular the glucose transporter-1 (GLUT1).

Di Chiro reported the clinical use of FDG-PET by showing the correlation between FDG uptake and the malignancy of cerebral tumors (66). These days, the vast majority of clinical PET studies use FDG, and its main applications include the staging and diagnosis of various malignancies, identification of metastatic lesions and monitoring of therapy (6,63,64). Among the many clinical studies done over the recent years, the most established and agreed upon are the staging of colorectal cancer, melanoma and lymphoma (67), lung cancers staging (64) and response to therapy (68).

Recently a near infra red analog of 2-deoxyglucose (IRDye800CW 2-DG; Li-Cor Biosciences, Lincoln, NB) was applied to allow optical imaging of glucose uptake in small animals (69).

Monitoring tumor glycolysis by magnetic resonance

^{1}H MRS was suggested for mapping lactate, the metabolic product of glycolysis (6). The response to chemotherapy, can be detected showing a decrease in lactate levels (70). However, ^{1}H spectra of metabolites are often obscured by the large water signal and the broad lipid resonances, thus presaturation of the water or fat resonances and phase cycling are added to the pulse program to eliminate the lipid signals (71).

Magic angle spinning (MAS) had enabled the study of ex-vivo biopsies of tumors and their metabolic profiles at high resolution. For example, using MAS of *ex-vivo* malignant lymph nodes, a correlation was found between lactate levels and histopatholgical grades (72,73).

^{13}C MRS is useful for evaluating the kinetics of some of the metabolic pathways in cancer, in particular, glycolysis. It is possible to determine the glycolysis rate by the rate of glucose conversion to lactate using ^{13}C MRS. However, these spectra will usually suffer from low SNR due to ^{13}C low natural abundance (64). The use of enriched ^{13}C substrates may help overcome this sensitivity issue, thus enabling the in-vivo measurements of glucose metabolism in tumors (74). Another technique to increase the SNR of the spectrum is by the indirect detection of ^{13}C through heteronuclear Cross Polarization between ^{1}H and ^{13}C (75). ^{13}C-CP was applied in C3H murine mammary carcinomas in-vivo to study the glycolytic rate under hypoxia, normoxia and hyperoxia. Glucose and lactate clearance rates, as well as apparent glycolytic rate were determined, demonstrating the increase in glycolysis with decrease in oxygenation, thus evaluating the relationship between oxygen status and energy metabolism (75).

Dynamic nuclear polarization (DNP) technique had enabled the hyperpolarization of ^{13}C labeled molecules, thus obtaining signal enhancements of >10,000 times (76). The DNP technique is based on the polarization of nuclear spins, at about 1 K, through their coupling with the unpaired electrons that are introduced through the labeled free radical. At such a low temperature, the high electron polarization is transferred to the nuclear spins by microwave irradiation (76).

Due to the high enhancement ratio, this new technique, together with the development of new ^{13}C-based probes, has provided the base for studies of metabolic fluxes in a few biochemical pathways (77-79). Hyperpolarized [1-^{13}C]-pyruvate was one of the first investigated biomarkers, because of its relatively long T_1 and its being a key factor in

several biochemical pathways (78). DNP studies performed in tumors have shown that the labeled pyruvate is converted into lactate, alanine and bicarbonate (Figure 3 C) (77-79).

The consequences of the increased glycolysis and lactate production is the reduced extracellular pH in cancer (6). The distribution of pH can be mapped elegantly by ^{13}C MRI using hyperpolarized bicarbonate (Figure 3 D) (80).

Application of DNP for analysis of tumor metabolism is limited by the decay of polarization with T1 relaxation, limiting the analysis to seconds after administration. This limitation may severely impact application particularly in regions of limited blood flow as expected for hypoxic regions of tumors.

Hypoxia and genetic stability

Tumor cells are exposed to fluctuating and chronically low level of oxygen thus, resulting in accumulation of DNA deletions and translocations (8). These alterations accumulation is due to the reduced DNA repair capacity under hypoxia (81,82).

Recently, the role of hypoxia regulated microRNAs mir-210 and mir-373, on the expression of DNA repair genes was demonstrated (83). Despite the importance of genetic instability to cancer, development of non-invasive imaging tools for detection of genetic instability remain a challenge.

Hypoxia induced angiogenesis: the role of VEGF

A major cellular response to hypoxic stress mediated by HIF-1 is the stimulation of VEGF (Figure 4 A). VEGF is a 34-46-kDa heparin-binding dimeric glycoprotein, which is specifically mitogenic for endothelial cells (84). The initial step in VEGF action is binding to either of two tyrosine kinase receptors, VEGFR-1 and VEGFR-2. VEGFR-2, however, is the main receptor involved in activation VEGF signal transduction cascade of intracellular events involving Raf/Mek/Erk (85) and phosphatidylinositol (PI)-3 kinase–Akt pathways. Thus, leading to integrin-mediated cell adhesion, growth, proliferation, migration, survival, and increased permeability of endothelial cells (86). The regulation of VEGF expression during tumor progression may involve diverse mechanisms in addition to hypoxia, including activated oncogenes, mutant or deleted tumor suppressor genes, cytokines and hormonal modulators (87).

Imaging of VEGF induced angiogenesis

Over the past years, there has been a surge in the development of MRI techniques studying tumor angiogenesis, with the main goal of monitoring the response to antiangiogenic therapy (88). VEGF is considered a main regulator involved in the development of new microvasculature thus many of the efforts over the past years have focused on the development of non-invasive, accurate and quantitative MRI techniques for monitoring the response to elevation in VEGF levels or to anti-VEGF treatment *in-vivo*. Since one of the early responses of VEGF stimulation is increased vascular permeability, DCE-MRI is considered to be one of the most effective techniques for the study of tumor angiogenesis (27,58,89-93).

DCE-MRI using the small molecular weight GdDTPA can detect changes in tumor microvasculature properties, and is considered one of the most common clinical techniques for monitoring changes in VEGF-induced permeability (94). Kinetic parameters such as the influx and efflux are derived from the T_1 relaxivity changes induced by the contrast agent and used to determine the extravascular extracellular volume fraction and transcapillary

transfer rates (95). The utility of these parameters in evaluating the efficiency of anti-VEGF treatment has been studied (96). However, due to their fast rate of extravasation also from normal vascular beds, low-molecular contrast agents are not ideal for studying vascular permeability in tumors.

Enhanced permeability, associated with VEGF stimulation, leads to the extravasation of plasma proteins, thus DCE-MRI using high-molecular-weight contrast agents can be used for increased sensitivity and specificity in detection of vessel permeability (89). Albumin-based contrast materials can be used to study tumor vascular volume fraction and vascular permeability, from the dynamic T_1 maps acquired before and after the administration of the contrast material (92).

Acute hyperpermeability induced by intradermal administration of VEGF165 was demonstrated using albumin based contrast material (biotin-BSA-GdDTPA) (97). Early local vasodilation and increased permeability in response to intradermal VEGF165 were detected. Accumulation of the contrast material followed a single exponential saturation behavior. Analysis of the saturation kinetics of contrast leak provided noninvasive quantification for the rapid kinetics of inactivation of VEGF in vivo (97). Chronic exposure to VEGF was found to be associated with increased blood volume (Figure 4 B), increased vessel permeability (Figure 4 C) and enhanced interstitial convection (Figure 4 D) (91).

The role of VEGF in vascular plasticity and the importance of vascular maturation in vascular resistance to VEGF withdrawal were measured by BOLD-contrast MRI (51). Switchable, VEGF-overexpressing tumors implemented in nude mice displayed high functionality as a response to hyperoxia with high VEGF levels. Upon VEGF withdrawal, only regions of immature blood vessels displayed significant vascular damage, whereas mature tumor vessels were resistant to VEGF withdrawal, and showed no signal changes in response to hypercapnia. This study demonstrated that VEGF is essential for survival of immature neovasculature (51).

MRI of albumin–gadolinium-DTPA was combined with optical imaging to clarify the relationship between vascular parameters and hypoxia (28,98). PC-3 human prostate cancer xenografts were engineered to express enhanced green fluorescent protein under control of hypoxia response element. Co-localized maps of vascular volume, permeability, and enhanced green fluorescent protein demonstrated that hypoxic regions were characterized by low vascular volume, and frequently by high permeability, consistent with hypoxia induced expression of VEGF (28).

Elevated interstitial fluid pressure, interstitial convection and lymphatic drain

One of the consequences of the elevated vascular permeability along with inflammation, lymphatic vessel abnormalities, fibrosis and contraction of the interstitial matrix is elevation of the interstitial fluid pressure (IFP) (99,100). DCE-MRI of orthotopically inoculated invasive breast tumors revealed a discrepancy in outward and inward fluxes of the contrast during tumor growth, with the outward exceeding the inward (101). Slow infusion of Gd-DTPA into the blood of mice transplanted with ectopic human lung tumors yielded images of the steady-state distribution of the contrast material, indicating that the transfer of GdDTPA in tumors may be regulated by IFP (102).

The effects of tumor vascular hyperpermeability, induced by overexpression of VEGF, on interstitial convection and lymphatic uptake were measured by DCE-MRI, confocal microscopy and histology, using albumin triple-labeled with biotin, fluorescein, and

GdDTPA (91). C6 glioma tumors engineered to overexpress VEGF165 under the switchable tetracycline regulation (C6-pTET-VEGF165). DCE-MRI was applied after i.v. administration of the contrast material, producing maps of blood plasma volume (fBV: Figure 4 B), vessel permeability (PSP; Figure 4 C) and interstitial convection (Time2max; Figure 4 D), which were confirmed by fluorescent microscopy and histology. In order to follow the lymphatic drain, avidin chase was applied, inducing rapid clearance of the intravascular biotinylated contrast material, providing experimental separation between vascular leak and lymphatic drain. This study demonstrated that VEGF stimulation increased not only vascular density and vascular hyperpermeability, but also interstitial convection and lymphatic drain.

Heparanase-dependent vascular changes in lymph nodes and the initial stages of lymph node infiltration were similarly detected by DCE-MRI following the administration of the triple labeled albumin (biotin-BSA-GdDTPA-FAM/ROX) (103). Heparanase-overexpressing subcutaneous Eb mouse T-lymphoma tumors showed elevated vascular permeability in the primary tumors as well as in the draining lymph nodes. Early enhancement was induced for those lymph nodes draining the primary tumors, and enhancement was further elevated for tumors overexpressing heparanase. These results further support the role of heparanase in tumor metastasis to sentinel lymph nodes (103).

Heparanase proangiogenic and prometastaic properties were investigated by BOLD-contrast MRI. Upon overexpression of a secreted form of heparanase in mouse lymphoma cells, increased vessel density and increased functionality was observed as a response to hyperoxia (104). The effects of lymphatic drain, revealed by delayed enhancement and drain in BSA-GdDTPA enhanced MRI and metastatic spread to sentinal lymphnodes was demonstrated also for breast tumors (98).

Hypoxia, oxidative stress and inflammation

Intermittent blood flow leading to exposure of tumor cells to acute hypoxia and reperfusion, along with the switch to glycolysis and changes in mitochondrial function, result in generation of reactive oxygen species (ROS). Exposure to ROS can contribute to the induction of inflammation, it can promote tumor cell invasion and it can stimulate lymphangiogenesis, thereby facilitating lymphnode metastatic spread (Figure 5 A).

The inflammation–cancer link can be viewed as a defense mechanism (tumor immunosurveillance) as well as tumor platform contributing to tumor initiation, growth and invasiveness. Infiltrated inflammatory cells, such as neutrophils, lymphocytes and macrophages help to establish a microenvironment promoting cancer development, whereas a malignant tumor feeds the inflammatory response and accelerates tumor growth. These infiltrated immune cells secrete cytokines, chemokines and growth factors, such as TNFα, TGFβ, IL-6, fibroblast growth factor (FGF) and epidermal growth factor (EGF) (105), which activate two key transcription factors NF-κB and STAT3 in response to microenvironmental stress (106). Activation of NFκB plays a central role in the activation of numerous proinflammatory cytokines in multiple cell types, including macrophages, T cells and epithelial cells. NFκB promotes cancer cell migration and metastasis induced expression of Bcl-2 to suppress apoptosis (107). Although STAT3 can be activated by various cytokines, growth factors and oncogenicmolecules, its constitutive expression is often found adjacent to infiltrated immune cells within the tumor (108). Furthermore inflammatory signals also regulate the production and activation of various proteases, which degrade extracellular matrix (ECM), and facilitate invasion and extravasation of cancer cells.

The recruitment of macrophages and other inflammatory cells to tumors can be followed by imaging using iron oxide labeling. Alternatively the cells can be labeled with NIR fluorescent dyes for fluorescence tomography (FMT; Figure 5 B) (109).

The pro-inflammatory environment in tumors stimulates cell motility and invasion. One of the effects is the secretion of matrix metalloproteinases (MMPs), a family of 23 zinc-containing endopeptidases that cleave a broad range of components of ECM, basement membrane, growth factors, and cell surface receptors (110). MMPs that are upregulated in cancer progression, can act as oncogenes, and promote invasion and metastasis in most solid tumors. MMPs are synthesized by a wide variety of cell types and are present in an inactive form as secreted or cell surface proteins. Their activation is mediated by proteinases, such as furin, plasmin (111) as well as by ROS (112). The predominant MMPs implicated in tumor progression are MMP-2, -9, and -14 (113). Analysis of the mechanisms involved in the tumor-induced angiogenic switch has identified MMP-9 as a major contributor due to its ability to break down basement membrane and release VEGF (114). Additionally, MMPs were shown to be involved both in the inflammation and lymphangiogenesis processes of the expending tumor (115). Imaging MMP activity in tumors was reported using a smart activatable NIR probe (116) (Figure 5 C).

Oxidative stress and lymphangiogenesis

Oxidative stress induces multiple stress pathways. Recently, the role of lens epithelium derived growth factor (LEDGF) was recognized as part of the response of mammalian cells to oxidative stress. LEDGF induces expression of its target genes either through activation of a stress response element (117) or by facilitating chromatin interaction of JPO2, the Myc-interacting protein (118). VEGF-C, the primary growth factor inducing lymphangiogenesis was implicated in lymph node metastasis in many cancers (119). VEGF-C mediates its effect through the VEGFR-3 receptor on lymphatic endothelial cells, shows LEDGF-induced expression in response to oxidative stress (as well as hormonal stimulation) (120,121). The promoter of VEGF-C includes a, STRE enhancer that is conserved in mammals and mediates LEDGF induced expression of VEGF-C. Intravital imaging demonstrated the expansion of the peritumor lymphatic bed in response to LEDGF over expression (120) (Figure 5 D).

Summary

Tumor cells evolve under selection pressure generated by the exhaustion of nutrient supply and the exposure to chronic and acute hypoxia. Under these conditions, tumor cells adopt a range of characteristic alterations that facilitate tumor progression and metastasis. Tumor hypoxia was associated with genetic instability, elevated glycolysis and angiogenesis, increased tumor acidosis and elevated interstitial pressure along with increased peritumor convection and lymphatic drain. The ability to non-invasively image the many changes associated with tumor hypoxia and its consequences, provides a critical role for imaging in preclinical research and in clinical assessment of tumor progression.

Acknowledgments

This work was supported by the Israel Science Foundation 93/07 (to M.N. and B.C.), by the DKFZ-MOST cooperational program, by National Institutes of Health grant R01 CA75334, by the European Commission 6th Framework Integrated Project MEDITRANS, by the European Commission 7th Framework Integrated Project ENCITE, by the 7th Framework European Research Council Advanced grant 232640-IMAGO (to M.N.). M.N. is incumbent of the Helen and Morris Mauerberger Chair in Biological Sciences.

Europe PMC Funders Author Manuscripts

Abbreviations

(FDG)	2-18F-fluoro-2-deoxy-D-glucose
(BNIP3)	Bcl-2/E1B-19K-interacting protein 3
(BOLD)	blood oxygen level-dependent
(DW)	Diffusion weighted
(DCE)	dynamic contrast enhanced
(DNP)	Dynamic nuclear polarization
(EPR)	electron paramagnetic resonance
(ECM)	extracellular matrix
(FMT)	fluorescence tomography
(FREDOM)	fluorocarbon relaxometry using echoplanar imaging for dynamic oxygen mapping
(GLUT1)	glucose transporter-1
(HFB)	Hexafluorobenzene
(HMDSO)	hexamethyldisiloxane
(HIF)	hypoxia-inducible factor
(HREs)	hypoxia-responsive-elements
(IFP)	interstitial fluid pressure
(LEDGF)	lens epithelium derived growth factor
(LiPc)	lithium phthalocyanine
(MAS)	Magic Angle Spinning
(MMPs)	matrix metalloproteinases
(OMRI)	Overhauser magnetic resonance imaging
(ODDD)	oxygen-dependent degradation domain
(PFCs)	Perfluorocarbons
(PET)	Positron emission tomography
(PHDs)	prolyl hydroxylases
(PEDRI)	proton electron double resonance imaging
(PISTOL)	proton imaging of siloxanes to map tissue oxygenation levels
(PDK1)	pyruvate dehydrogenase kinase 1
(ROS)	reactive oxygen species
(RBC)	red blood cells
(SNR)	signal to noise ratio
(TCA)	tricarboxylic acid
(VEGF)	vascular endothelial growth factor
(VHL)	von Hippel-Lindau
(WT)	wildtype

References

1. Hanahan D, Weinberg RA. The hallmarks of cancer. Cell. 2000; 100(1):57–70. [PubMed: 10647931]
2. Warburg O. On respiratory impairment in cancer cells. Science. 1956; 124(3215):269–270. [PubMed: 13351639]
3. Warburg O. On the origin of cancer cells. Science. 1956; 123(3191):309–314. [PubMed: 13298683]
4. Hsu PP, Sabatini DM. Cancer cell metabolism: Warburg and beyond. Cell. 2008; 134(5):703–707. [PubMed: 18775299]
5. Milosevic M, Fyles A, Hedley D, Hill R. The human tumor microenvironment: invasive (needle) measurement of oxygen and interstitial fluid pressure. Semin Radiat Oncol. 2004; 14(3):249–258. [PubMed: 15254868]
6. Gatenby RA, Gillies RJ. Why do cancers have high aerobic glycolysis? Nat Rev Cancer. 2004; 4(11):891–899. [PubMed: 15516961]
7. Secomb TW, Hsu R, Dewhirst MW, Klitzman B, Gross JF. Analysis of oxygen transport to tumor tissue by microvascular networks. Int J Radiat Oncol Biol Phys. 1993; 25(3):481–489. [PubMed: 8436527]
8. Reynolds TY, Rockwell S, Glazer PM. Genetic instability induced by the tumor microenvironment. Cancer Res. 1996; 56(24):5754–5757. [PubMed: 8971187]
9. Vaupel P. Tumor microenvironmental physiology and its implications for radiation oncology. Semin Radiat Oncol. 2004; 14(3):198–206. [PubMed: 15254862]
10. Vaupel P, Mayer A. Hypoxia in cancer: significance and impact on clinical outcome. Cancer Metastasis Rev. 2007; 26(2):225–239. [PubMed: 17440684]
11. Tatum JL, Kelloff GJ, Gillies RJ, Arbeit JM, Brown JM, Chao KS, Chapman JD, Eckelman WC, Fyles AW, Giaccia AJ, Hill RP, Koch CJ, Krishna MC, Krohn KA, Lewis JS, Mason RP, Melillo G, Padhani AR, Powis G, Rajendran JG, Reba R, Robinson SP, Semenza GL, Swartz HM, Vaupel P, Yang D, Croft B, Hoffman J, Liu G, Stone H, Sullivan D. Hypoxia: importance in tumor biology, noninvasive measurement by imaging, and value of its measurement in the management of cancer therapy. Int J Radiat Biol. 2006; 82(10):699–757. [PubMed: 17118889]
12. Vikram DS, Zweier JL, Kuppusamy P. Methods for noninvasive imaging of tissue hypoxia. Antioxid Redox Signal. 2007; 9(10):1745–1756. [PubMed: 17663644]
13. Krohn KA, Link JM, Mason RP. Molecular imaging of hypoxia. J Nucl Med. 2008; 49(Suppl 2): 129S–148S. [PubMed: 18523070]
14. Khan N, Williams BB, Hou H, Li H, Swartz HM. Repetitive tissue pO2 measurements by electron paramagnetic resonance oximetry: current status and future potential for experimental and clinical studies. Antioxid Redox Signal. 2007; 9(8):1169–1182. [PubMed: 17536960]
15. Gallez B, Baudelet C, Jordan BF. Assessment of tumor oxygenation by electron paramagnetic resonance: principles and applications. NMR Biomed. 2004; 17(5):240–262. [PubMed: 15366026]
16. Swartz HM, Clarkson RB. The measurement of oxygen in vivo using EPR techniques. Phys Med Biol. 1998; 43(7):1957–1975. [PubMed: 9703059]
17. Halpern HJ, Yu C, Peric M, Barth E, Grdina DJ, Teicher BA. Oxymetry deep in tissues with low-frequency electron paramagnetic resonance. Proc Natl Acad Sci U S A. 1994; 91(26):13047–13051. [PubMed: 7809170]
18. Gallez B, Bacic G, Goda F, Jiang J, O'Hara JA, Dunn JF, Swartz HM. Use of nitroxides for assessing perfusion, oxygenation, and viability of tissues: in vivo EPR and MRI studies. Magn Reson Med. 1996; 35(1):97–106. [PubMed: 8771027]
19. Khan FA, Khan M, Abbasi S. Arterial to end-tidal carbon dioxide difference in neurosurgical patients undergoing craniotomy: a review of practice. J Pak Med Assoc. 2007; 57(9):446–448. [PubMed: 18072639]
20. Elas M, Williams BB, Parasca A, Mailer C, Pelizzari CA, Lewis MA, River JN, Karczmar GS, Barth ED, Halpern HJ. Quantitative tumor oxymetric images from 4D electron paramagnetic resonance imaging (EPRI): methodology and comparison with blood oxygen level-dependent (BOLD) MRI. Magn Reson Med. 2003; 49(4):682–691. [PubMed: 12652539]

21. Khan N, Li H, Hou H, Lariviere JP, Gladstone DJ, Demidenko E, Swartz HM. Tissue pO2 of orthotopic 9L and C6 gliomas and tumor-specific response to radiotherapy and hyperoxygenation. Int J Radiat Oncol Biol Phys. 2009; 73(3):878–885. [PubMed: 19136221]
22. Khan N, Mupparaju SP, Hou H, Lariviere JP, Demidenko E, Swartz HM, Eastman A. Radiotherapy in conjunction with 7-hydroxystaurosporine: a multimodal approach with tumor pO2 as a potential marker of therapeutic response. Radiat Res. 2009; 172(5):592–597. [PubMed: 19883227]
23. Williams BB, Hou H, Grinberg OY, Demidenko E, Swartz HM. High spatial resolution multisite EPR oximetry of transient focal cerebral ischemia in the rat. Antioxid Redox Signal. 2007; 9(10): 1691–1698. [PubMed: 17678442]
24. Salikhov I, Walczak T, Lesniewski P, Khan N, Iwasaki A, Comi R, Buckey J, Swartz HM. EPR spectrometer for clinical applications. Magn Reson Med. 2005; 54(5):1317–1320. [PubMed: 16193470]
25. Guiberteau T, Grucker D. Dynamic nuclear polarization imaging in very low magnetic fields as a noninvasive technique for oximetry. J Magn Reson. 1997; 124(1):263–266. [PubMed: 9424314]
26. Krishna MC, English S, Yamada K, Yoo J, Murugesan R, Devasahayam N, Cook JA, Golman K, Ardenkjaer-Larsen JH, Subramanian S, Mitchell JB. Overhauser enhanced magnetic resonance imaging for tumor oximetry: coregistration of tumor anatomy and tissue oxygen concentration. Proc Natl Acad Sci U S A. 2002; 99(4):2216–2221. [PubMed: 11854518]
27. Matsumoto S, Yasui H, Batra S, Kinoshita Y, Bernardo M, Munasinghe JP, Utsumi H, Choudhuri R, Devasahayam N, Subramanian S, Mitchell JB, Krishna MC. Simultaneous imaging of tumor oxygenation and microvascular permeability using Overhauser enhanced MRI. Proc Natl Acad Sci U S A. 2009; 106(42):17898–17903. [PubMed: 19815528]
28. Raman V, Artemov D, Pathak AP, Winnard PT Jr. McNutt S, Yudina A, Bogdanov A Jr. Bhujwalla ZM. Characterizing vascular parameters in hypoxic regions: a combined magnetic resonance and optical imaging study of a human prostate cancer model. Cancer Res. 2006; 66(20): 9929–9936. [PubMed: 17047055]
29. Penet MF, Pathak AP, Raman V, Ballesteros P, Artemov D, Bhujwalla ZM. Noninvasive multiparametric imaging of metastasis-permissive microenvironments in a human prostate cancer xenograft. Cancer Res. 2009; 69(22):8822–8829. [PubMed: 19861534]
30. Robinson SP, Griffiths JR. Current issues in the utility of 19F nuclear magnetic resonance methodologies for the assessment of tumour hypoxia. Philos Trans R Soc Lond B Biol Sci. 2004; 359(1446):987–996. [PubMed: 15306411]
31. Yu JX, Kodibagkar VD, Cui W, Mason RP. 19F: a versatile reporter for non-invasive physiology and pharmacology using magnetic resonance. Curr Med Chem. 2005; 12(7):819–848. [PubMed: 15853714]
32. Zhao D, Jiang L, Mason RP. Measuring changes in tumor oxygenation. Methods Enzymol. 2004; 386:378–418. [PubMed: 15120262]
33. Mason RP, Constantinescu A, Hunjan S, Le D, Hahn EW, Antich PP, Blum C, Peschke P. Regional tumor oxygenation and measurement of dynamic changes. Radiat Res. 1999; 152(3): 239–249. [PubMed: 10453084]
34. Xia M, Kodibagkar V, Liu H, Mason RP. Tumour oxygen dynamics measured simultaneously by near-infrared spectroscopy and 19F magnetic resonance imaging in rats. Phys Med Biol. 2006; 51(1):45–60. [PubMed: 16357430]
35. Zhao D, Ran S, Constantinescu A, Hahn EW, Mason RP. Tumor oxygen dynamics: correlation of in vivo MRI with histological findings. Neoplasia. 2003; 5(4):308–318. [PubMed: 14511402]
36. Bourke VA, Zhao D, Gilio J, Chang CH, Jiang L, Hahn EW, Mason RP. Correlation of radiation response with tumor oxygenation in the Dunning prostate R3327-AT1 tumor. Int J Radiat Oncol Biol Phys. 2007; 67(4):1179–1186. [PubMed: 17336219]
37. Jordan BF, Cron GO, Gallez B. Rapid monitoring of oxygenation by 19F magnetic resonance imaging: Simultaneous comparison with fluorescence quenching. Magn Reson Med. 2009; 61(3): 634–638. [PubMed: 19097235]

38. Kodibagkar VD, Wang X, Pacheco-Torres J, Gulaka P, Mason RP. Proton imaging of siloxanes to map tissue oxygenation levels (PISTOL): a tool for quantitative tissue oximetry. NMR Biomed. 2008; 21(8):899–907. [PubMed: 18574806]
39. Kodibagkar VD, Cui W, Merritt ME, Mason RP. Novel 1H NMR approach to quantitative tissue oximetry using hexamethyldisiloxane. Magn Reson Med. 2006; 55(4):743–748. [PubMed: 16506157]
40. Semenza GL. HIF-1 and mechanisms of hypoxia sensing. Curr Opin Cell Biol. 2001; 13(2):167–171. [PubMed: 11248550]
41. Huang J, Zhao Q, Mooney SM, Lee FS. Sequence determinants in hypoxia-inducible factor-1alpha for hydroxylation by the prolyl hydroxylases PHD1, PHD2, and PHD3. J Biol Chem. 2002; 277(42):39792–39800. [PubMed: 12181324]
42. Maxwell PH, Wiesener MS, Chang GW, Clifford SC, Vaux EC, Cockman ME, Wykoff CC, Pugh CW, Maher ER, Ratcliffe PJ. The tumour suppressor protein VHL targets hypoxia-inducible factors for oxygen-dependent proteolysis. Nature. 1999; 399(6733):271–275. [PubMed: 10353251]
43. Semenza GL. Targeting HIF-1 for cancer therapy. Nat Rev Cancer. 2003; 3(10):721–732. [PubMed: 13130303]
44. Bardos JI, Ashcroft M. Hypoxia-inducible factor-1 and oncogenic signalling. Bioessays. 2004; 26(3):262–269. [PubMed: 14988927]
45. Vaupel P, Hockel M, Mayer A. Detection and characterization of tumor hypoxia using pO2 histography. Antioxid Redox Signal. 2007; 9(8):1221–1235. [PubMed: 17536958]
46. Ryan HE, Poloni M, McNulty W, Elson D, Gassmann M, Arbeit JM, Johnson RS. Hypoxia-inducible factor-1alpha is a positive factor in solid tumor growth. Cancer Res. 2000; 60(15):4010–4015. [PubMed: 10945599]
47. Liao D, Corle C, Seagroves TN, Johnson RS. Hypoxia-inducible factor-1alpha is a key regulator of metastasis in a transgenic model of cancer initiation and progression. Cancer Res. 2007; 67(2): 563–572. [PubMed: 17234764]
48. Ogawa S, Lee TM. Magnetic resonance imaging of blood vessels at high fields: in vivo and in vitro measurements and image simulation. Magn Reson Med. 1990; 16(1):9–18. [PubMed: 2255240]
49. Ogawa S, Lee TM, Kay AR, Tank DW. Brain magnetic resonance imaging with contrast dependent on blood oxygenation. Proc Natl Acad Sci U S A. 1990; 87(24):9868–9872. [PubMed: 2124706]
50. Thulborn KR, Waterton JC, Matthews PM, Radda GK. Oxygenation dependence of the transverse relaxation time of water protons in whole blood at high field. Biochim Biophys Acta. 1982; 714(2):265–270. [PubMed: 6275909]
51. Abramovitch R, Dafni H, Smouha E, Benjamin LE, Neeman M. In vivo prediction of vascular susceptibility to vascular susceptibility endothelial growth factor withdrawal: magnetic resonance imaging of C6 rat glioma in nude mice. Cancer Res. 1999; 59(19):5012–5016. [PubMed: 10519416]
52. Neeman M, Dafni H, Bukhari O, Braun RD, Dewhirst MW. In vivo BOLD contrast MRI mapping of subcutaneous vascular function and maturation: validation by intravital microscopy. Magn Reson Med. 2001; 45(5):887–898. [PubMed: 11323816]
53. Gilead A, Meir G, Neeman M. The role of angiogenesis, vascular maturation, regression and stroma infiltration in dormancy and growth of implanted MLS ovarian carcinoma spheroids. Int J Cancer. 2004; 108(4):524–531. [PubMed: 14696116]
54. Gilad AA, Israely T, Dafni H, Meir G, Cohen B, Neeman M. Functional and molecular mapping of uncoupling between vascular permeability and loss of vascular maturation in ovarian carcinoma xenografts: the role of stroma cells in tumor angiogenesis. Int J Cancer. 2005; 117(2):202–211. [PubMed: 15880497]
55. Carmeliet P, Dor Y, Herbert JM, Fukumura D, Brusselmans K, Dewerchin M, Neeman M, Bono F, Abramovitch R, Maxwell P, Koch CJ, Ratcliffe P, Moons L, Jain RK, Collen D, Keshert E. Role of HIF-1alpha in hypoxia-mediated apoptosis, cell proliferation and tumour angiogenesis. Nature. 1998; 394(6692):485–490. [PubMed: 9697772]

56. Griffiths JR, McSheehy PM, Robinson SP, Troy H, Chung YL, Leek RD, Williams KJ, Stratford IJ, Harris AL, Stubbs M. Metabolic changes detected by in vivo magnetic resonance studies of HEPA-1 wild-type tumors and tumors deficient in hypoxia-inducible factor-1beta (HIF-1beta): evidence of an anabolic role for the HIF-1 pathway. Cancer Res. 2002; 62(3):688–695. [PubMed: 11830521]
57. Gross DJ, Reibstein I, Weiss L, Slavin S, Dafni H, Neeman M, Pines M, Nagler A. Treatment with halofuginone results in marked growth inhibition of a von Hippel-Lindau pheochromocytoma in vivo. Clin Cancer Res. 2003; 9(10 Pt 1):3788–3793. [PubMed: 14506172]
58. Jordan BF, Runquist M, Raghunand N, Baker A, Williams R, Kirkpatrick L, Powis G, Gillies RJ. Dynamic contrast-enhanced and diffusion MRI show rapid and dramatic changes in tumor microenvironment in response to inhibition of HIF-1alpha using PX-478. Neoplasia. 2005; 7(5): 475–485. [PubMed: 15967100]
59. Brown GK. Glucose transporters: structure, function and consequences of deficiency. J Inherit Metab Dis. 2000; 23(3):237–246. [PubMed: 10863940]
60. Semenza GL, Jiang BH, Leung SW, Passantino R, Concordet JP, Maire P, Giallongo A. Hypoxia response elements in the aldolase A, enolase 1, and lactate dehydrogenase A gene promoters contain essential binding sites for hypoxia-inducible factor 1. J Biol Chem. 1996; 271(51):32529–32537. [PubMed: 8955077]
61. Kim JW, Tchernyshyov I, Semenza GL, Dang CV. HIF-1-mediated expression of pyruvate dehydrogenase kinase: a metabolic switch required for cellular adaptation to hypoxia. Cell Metab. 2006; 3(3):177–185. [PubMed: 16517405]
62. Zhang H, Bosch-Marce M, Shimoda LA, Tan YS, Baek JH, Wesley JB, Gonzalez FJ, Semenza GL. Mitochondrial autophagy is an HIF-1-dependent adaptive metabolic response to hypoxia. J Biol Chem. 2008; 283(16):10892–10903. [PubMed: 18281291]
63. Gambhir SS. Molecular imaging of cancer with positron emission tomography. Nat Rev Cancer. 2002; 2(9):683–693. [PubMed: 12209157]
64. Czernin J, Phelps ME. Positron emission tomography scanning: current and future applications. Annu Rev Med. 2002; 53:89–112. [PubMed: 11818465]
65. Catana C, Procissi D, Wu Y, Judenhofer MS, Qi J, Pichler BJ, Jacobs RE, Cherry SR. Simultaneous in vivo positron emission tomography and magnetic resonance imaging. Proc Natl Acad Sci U S A. 2008; 105(10):3705–3710. [PubMed: 18319342]
66. Di Chiro G. Positron emission tomography using [18F] fluorodeoxyglucose in brain tumors. A powerful diagnostic and prognostic tool. Invest Radiol. 1987; 22(5):360–371. [PubMed: 3496318]
67. Delbeke D. Oncological applications of FDG PET imaging: brain tumors, colorectal cancer, lymphoma and melanoma. J Nucl Med. 1999; 40(4):591–603. [PubMed: 10210218]
68. Mac Manus M, Hicks RJ. The use of positron emission tomography (PET) in the staging/evaluation, treatment, and follow-up of patients with lung cancer: a critical review. Int J Radiat Oncol Biol Phys. 2008; 72(5):1298–1306. [PubMed: 19028270]
69. Zhou H, Luby-Phelps K, Mickey BE, Habib AA, Mason RP, Zhao D. Dynamic near-infrared optical imaging of 2-deoxyglucose uptake by intracranial glioma of athymic mice. PLoS One. 2009; 4(11):e8051. [PubMed: 19956682]
70. Aboagye EO, Bhujwalla ZM, Shungu DC, Glickson JD. Detection of tumor response to chemotherapy by 1H nuclear magnetic resonance spectroscopy: effect of 5-fluorouracil on lactate levels in radiation-induced fibrosarcoma 1 tumors. Cancer Res. 1998; 58(5):1063–1067. [PubMed: 9500472]
71. Pathak AP, Gimi B, Glunde K, Ackerstaff E, Artemov D, Bhujwalla ZM. Molecular and functional imaging of cancer: advances in MRI and MRS. Methods Enzymol. 2004; 386:3–60. [PubMed: 15120245]
72. Ronen SM, Volk A, Mispelter J. Comparative NMR study of a differentiated rat hepatoma and its dedifferentiated subclone cultured as spheroids and as implanted tumors. NMR Biomed. 1994; 7(6):278–286. [PubMed: 7841024]
73. Ross BD, Higgins RJ, Boggan JE, Willis JA, Knittel B, Unger SW. Carbohydrate metabolism of the rat C6 glioma. An in vivo 13C and in vitro 1H magnetic resonance spectroscopy study. NMR Biomed. 1988; 1(1):20–26. [PubMed: 3275020]

74. Cheng LL, Lean CL, Bogdanova A, Wright SC Jr. Ackerman JL, Brady TJ, Garrido L. Enhanced resolution of proton NMR spectra of malignant lymph nodes using magic-angle spinning. Magn Reson Med. 1996; 36(5):653–658. [PubMed: 8916014]
75. Nielsen FU, Daugaard P, Bentzen L, Stodkilde-Jorgensen H, Overgaard J, Horsman MR, Maxwell RJ. Effect of changing tumor oxygenation on glycolytic metabolism in a murine C3H mammary carcinoma assessed by in vivo nuclear magnetic resonance spectroscopy. Cancer Res. 2001; 61(13):5318–5325. [PubMed: 11431377]
76. Ardenkjaer-Larsen JH, Fridlund B, Gram A, Hansson G, Hansson L, Lerche MH, Servin R, Thaning M, Golman K. Increase in signal-to-noise ratio of > 10,000 times in liquid-state NMR. Proc Natl Acad Sci U S A. 2003; 100(18):10158–10163. [PubMed: 12930897]
77. Golman K, Ardenkjaer-Larsen JH, Petersson JS, Mansson S, Leunbach I. Molecular imaging with endogenous substances. Proc Natl Acad Sci U S A. 2003; 100(18):10435–10439. [PubMed: 12930896]
78. Golman K, Zandt RI, Lerche M, Pehrson R, Ardenkjaer-Larsen JH. Metabolic imaging by hyperpolarized 13C magnetic resonance imaging for in vivo tumor diagnosis. Cancer Res. 2006; 66(22):10855–10860. [PubMed: 17108122]
79. Kohler SJ, Yen Y, Wolber J, Chen AP, Albers MJ, Bok R, Zhang V, Tropp J, Nelson S, Vigneron DB, Kurhanewicz J, Hurd RE. In vivo 13 carbon metabolic imaging at 3T with hyperpolarized 13C-1-pyruvate. Magn Reson Med. 2007; 58(1):65–69. [PubMed: 17659629]
80. Gallagher FA, Kettunen MI, Day SE, Hu DE, Ardenkjaer-Larsen JH, Zandt R, Jensen PR, Karlsson M, Golman K, Lerche MH, Brindle KM. Magnetic resonance imaging of pH in vivo using hyperpolarized 13C-labelled bicarbonate. Nature. 2008; 453(7197):940–943. [PubMed: 18509335]
81. Mihaylova VT, Bindra RS, Yuan J, Campisi D, Narayanan L, Jensen R, Giordano F, Johnson RS, Rockwell S, Glazer PM. Decreased expression of the DNA mismatch repair gene Mlh1 under hypoxic stress in mammalian cells. Mol Cell Biol. 2003; 23(9):3265–3273. [PubMed: 12697826]
82. Yuan J, Narayanan L, Rockwell S, Glazer PM. Diminished DNA repair and elevated mutagenesis in mammalian cells exposed to hypoxia and low pH. Cancer Res. 2000; 60(16):4372–4376. [PubMed: 10969780]
83. Crosby ME, Kulshreshtha R, Ivan M, Glazer PM. MicroRNA regulation of DNA repair gene expression in hypoxic stress. Cancer Res. 2009; 69(3):1221–1229. [PubMed: 19141645]
84. Senger DR, Perruzzi CA, Feder J, Dvorak HF. A highly conserved vascular permeability factor secreted by a variety of human and rodent tumor cell lines. Cancer Res. 1986; 46(11):5629–5632. [PubMed: 3756910]
85. Takahashi T, Ueno H, Shibuya M. VEGF activates protein kinase C-dependent, but Ras-independent Raf-MEK-MAP kinase pathway for DNA synthesis in primary endothelial cells. Oncogene. 1999; 18(13):2221–2230. [PubMed: 10327068]
86. Ferrara N, Gerber HP, LeCouter J. The biology of VEGF and its receptors. Nat Med. 2003; 9(6): 669–676. [PubMed: 12778165]
87. Claffey KP, Robinson GS. Regulation of VEGF/VPF expression in tumor cells: consequences for tumor growth and metastasis. Cancer Metastasis Rev. 1996; 15(2):165–176. [PubMed: 8842488]
88. Neeman M, Dafni H. Structural, functional, and molecular MR imaging of the microvasculature. Annu Rev Biomed Eng. 2003; 5:29–56. [PubMed: 14527310]
89. Bhujwalla ZM, Artemov D, Glockner J. Tumor angiogenesis, vascularization, and contrast-enhanced magnetic resonance imaging. Top Magn Reson Imaging. 1999; 10(2):92–103. [PubMed: 10551624]
90. Brasch R, Pham C, Shames D, Roberts T, van Dijke K, van Bruggen N, Mann J, Ostrowitzki S, Melnyk O. Assessing tumor angiogenesis using macromolecular MR imaging contrast media. J Magn Reson Imaging. 1997; 7(1):68–74. [PubMed: 9039595]
91. Dafni H, Israely T, Bhujwalla ZM, Benjamin LE, Neeman M. Overexpression of vascular endothelial growth factor 165 drives peritumor interstitial convection and induces lymphatic drain: magnetic resonance imaging, confocal microscopy, and histological tracking of triple-labeled albumin. Cancer Res. 2002; 62(22):6731–6739. [PubMed: 12438274]

92. Demsar F, Roberts TP, Schwickert HC, Shames DM, van Dijke CF, Mann JS, Saeed M, Brasch RC. A MRI spatial mapping technique for microvascular permeability and tissue blood volume based on macromolecular contrast agent distribution. Magn Reson Med. 1997; 37(2):236–242. [PubMed: 9001148]

93. Pham CD, Roberts TP, van Bruggen N, Melnyk O, Mann J, Ferrara N, Cohen RL, Brasch RC. Magnetic resonance imaging detects suppression of tumor vascular permeability after administration of antibody to vascular endothelial growth factor. Cancer Invest. 1998; 16(4):225–230. [PubMed: 9589031]

94. Leach MO, Brindle KM, Evelhoch JL, Griffiths JR, Horsman MR, Jackson A, Jayson G, Judson IR, Knopp MV, Maxwell RJ, McIntyre D, Padhani AR, Price P, Rathbone R, Rustin G, Tofts PS, Tozer GM, Vennart W, Waterton JC, Williams SR, Workman P. Assessment of antiangiogenic and antivascular therapeutics using MRI: recommendations for appropriate methodology for clinical trials. Br J Radiol. 2003; 76(Spec No 1):S87–91. [PubMed: 15456718]

95. Tofts PS. Modeling tracer kinetics in dynamic Gd-DTPA MR imaging. J Magn Reson Imaging. 1997; 7(1):91–101. [PubMed: 9039598]

96. Jayson GC, Zweit J, Jackson A, Mulatero C, Julyan P, Ranson M, Broughton L, Wagstaff J, Hakannson L, Groenewegen G, Bailey J, Smith N, Hastings D, Lawrance J, Haroon H, Ward T, McGown AT, Tang M, Levitt D, Marreaud S, Lehmann FF, Herold M, Zwierzina H. Molecular imaging and biological evaluation of HuMV833 anti-VEGF antibody: implications for trial design of antiangiogenic antibodies. J Natl Cancer Inst. 2002; 94(19):1484–1493. [PubMed: 12359857]

97. Dafni H, Landsman L, Schechter B, Kohen F, Neeman M. MRI and fluorescence microscopy of the acute vascular response to VEGF165: vasodilation, hyper-permeability and lymphatic uptake, followed by rapid inactivation of the growth factor. NMR Biomed. 2002; 15(2):120–131. [PubMed: 11870908]

98. Pathak AP, Artemov D, Neeman M, Bhujwalla ZM. Lymph node metastasis in breast cancer xenografts is associated with increased regions of extravascular drain, lymphatic vessel area, and invasive phenotype. Cancer Res. 2006; 66(10):5151–5158. [PubMed: 16707438]

99. Jain RK. The next frontier of molecular medicine: delivery of therapeutics. Nat Med. 1998; 4(6): 655–657. [PubMed: 9623964]

100. Heldin CH, Rubin K, Pietras K, Ostman A. High interstitial fluid pressure - an obstacle in cancer therapy. Nat Rev Cancer. 2004; 4(10):806–813. [PubMed: 15510161]

101. Dadiani M, Margalit R, Sela N, Degani H. High-resolution magnetic resonance imaging of disparities in the transcapillary transfer rates in orthotopically inoculated invasive breast tumors. Cancer Res. 2004; 64(9):3155–3161. [PubMed: 15126354]

102. Hassid Y, Furman-Haran E, Margalit R, Eilam R, Degani H. Noninvasive magnetic resonance imaging of transport and interstitial fluid pressure in ectopic human lung tumors. Cancer Res. 2006; 66(8):4159–4166. [PubMed: 16618737]

103. Dafni H, Cohen B, Ziv K, Israely T, Goldshmidt O, Nevo N, Harmelin A, Vlodavsky I, Neeman M. The role of heparanase in lymph node metastatic dissemination: dynamic contrast-enhanced MRI of Eb lymphoma in mice. Neoplasia. 2005; 7(3):224–233. [PubMed: 15799822]

104. Goldshmidt O, Zcharia E, Abramovitch R, Metzger S, Aingorn H, Friedmann Y, Schirrmacher V, Mitrani E, Vlodavsky I. Cell surface expression and secretion of heparanase markedly promote tumor angiogenesis and metastasis. Proc Natl Acad Sci U S A. 2002; 99(15):10031–10036. [PubMed: 12097647]

105. Joyce JA, Pollard JW. Microenvironmental regulation of metastasis. Nat Rev Cancer. 2009; 9(4): 239–252. [PubMed: 19279573]

106. Grivennikov SI, Karin M. Dangerous liaisons: STAT3 and NF-kappaB collaboration and crosstalk in cancer. Cytokine Growth Factor Rev. 2010; 21(1):11–19. [PubMed: 20018552]

107. Karin M. Nuclear factor-kappaB in cancer development and progression. Nature. 2006; 441(7092):431–436. [PubMed: 16724054]

108. Groner B, Lucks P, Borghouts C. The function of Stat3 in tumor cells and their microenvironment. Semin Cell Dev Biol. 2008; 19(4):341–350. [PubMed: 18621135]

109. Leimgruber A, Berger C, Cortez-Retamozo V, Etzrodt M, Newton AP, Waterman P, Figueiredo JL, Kohler RH, Elpek N, Mempel TR, Swirski FK, Nahrendorf M, Weissleder R, Pittet MJ.

Behavior of endogenous tumor-associated macrophages assessed in vivo using a functionalized nanoparticle. Neoplasia. 2009; 11(5):459–468. 452 p following 468. [PubMed: 19412430]

110. Egeblad M, Werb Z. New functions for the matrix metalloproteinases in cancer progression. Nat Rev Cancer. 2002; 2(3):161–174. [PubMed: 11990853]
111. Sternlicht MD, Werb Z. How matrix metalloproteinases regulate cell behavior. Annu Rev Cell Dev Biol. 2001; 17:463–516. [PubMed: 11687497]
112. Fu X, Kassim SY, Parks WC, Heinecke JW. Hypochlorous acid generated by myeloperoxidase modifies adjacent tryptophan and glycine residues in the catalytic domain of matrix metalloproteinase-7 (matrilysin): an oxidative mechanism for restraining proteolytic activity during inflammation. J Biol Chem. 2003; 278(31):28403–28409. [PubMed: 12759346]
113. Littlepage LE, Sternlicht MD, Rougier N, Phillips J, Gallo E, Yu Y, Williams K, Brenot A, Gordon JI, Werb Z. Matrix metalloproteinases contribute distinct roles in neuroendocrine prostate carcinogenesis, metastasis, and angiogenesis progression. Cancer Res. 2010; 70(6): 2224–2234. [PubMed: 20215503]
114. Bergers G, Brekken R, McMahon G, Vu TH, Itoh T, Tamaki K, Tanzawa K, Thorpe P, Itohara S, Werb Z, Hanahan D. Matrix metalloproteinase-9 triggers the angiogenic switch during carcinogenesis. Nat Cell Biol. 2000; 2(10):737–744. [PubMed: 11025665]
115. Kessenbrock K, Plaks V, Werb Z. Matrix metalloproteinases: regulators of the tumor microenvironment. Cell. 2010; 141(1):52–67. [PubMed: 20371345]
116. Bremer C, Tung CH, Weissleder R. In vivo molecular target assessment of matrix metalloproteinase inhibition. Nat Med. 2001; 7(6):743–748. [PubMed: 11385514]
117. Singh DP, Fatma N, Kimura A, Chylack LT Jr. Shinohara T. LEDGF binds to heat shock and stress-related element to activate the expression of stress-related genes. Biochem Biophys Res Commun. 2001; 283(4):943–955. [PubMed: 11350077]
118. Maertens GN, Cherepanov P, Engelman A. Transcriptional co-activator p75 binds and tethers the Myc-interacting protein JPO2 to chromatin. J Cell Sci. 2006; 119(Pt 12):2563–2571. [PubMed: 16735438]
119. Tammela T, Alitalo K. Lymphangiogenesis: Molecular mechanisms and future promise. Cell. 2010; 140(4):460–476. [PubMed: 20178740]
120. Cohen B, Addadi Y, Sapoznik S, Meir G, Kalchenko V, Harmelin A, Ben-Dor S, Neeman M. Transcriptional regulation of vascular endothelial growth factor C by oxidative and thermal stress is mediated by lens epithelium-derived growth factor/p75. Neoplasia. 2009; 11(9):921–933. [PubMed: 19724686]
121. Sapoznik S, Cohen B, Tzuman Y, Meir G, Ben-Dor S, Harmelin A, Neeman M. Gonadotropin-regulated lymphangiogenesis in ovarian cancer is mediated by LEDGF-induced expression of VEGF-C. Cancer Res. 2009; 69(24):9306–9314. [PubMed: 19934313]

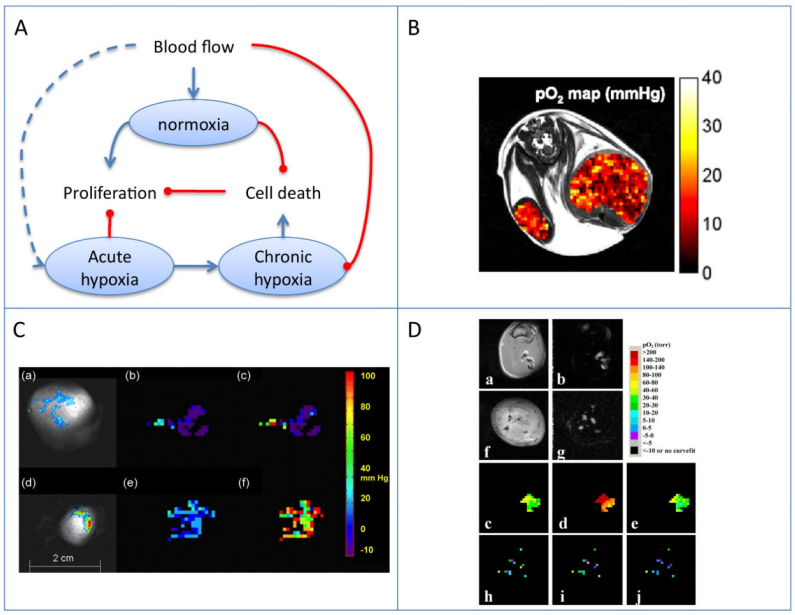

Figure 1.

Blood flow and tumor hypoxia.

A) Scheme showing the dynamic interaction of tumor perfusion, cell proliferation and cell death. Oxygen variation between normoxia, and chronic and acute hypoxia affect tumor progression through multiple mechanisms. B) EPR oximetry . Regional tissue pO_2 from an SCC tumor-bearing mouse obtained by OMRI at 0.015 mT overlaid on a 7-T MRI. FOV = 32 mm. Reproduced from (27).

C) 19F MR oximetry. Partial pressure of oxygen (pO_2) maps obtained using FREDOM (fluorocarbon relaxometry using echo planar imaging for dynamic oxygen mapping). Large tumor (3.6 cm^3; a-c), and a small tumor (1 cm^3; d-f). (a, d) Colorscale of 19F derived hexafluorobenzene distribution. (b, e) pO_2 maps during air breathing. (c, f) pO_2 maps after 24 min oxygen breathing. Reproduced from (36).

D) 1H MR 'PISTOL' oximetry, showing pO2 maps of rat thigh muscle (a-e) and Dunning prostate R3327 prostate MAT-Lu tumors (f-j) . (b, g) CHESS spin-echo images showing the distribution of the injected HMDSO. The corresponding time course PISTOL pO_2 maps (c, h, air; d, i, 30 min oxygen; e, j, 30 min after return to air). Reproduced from (38).

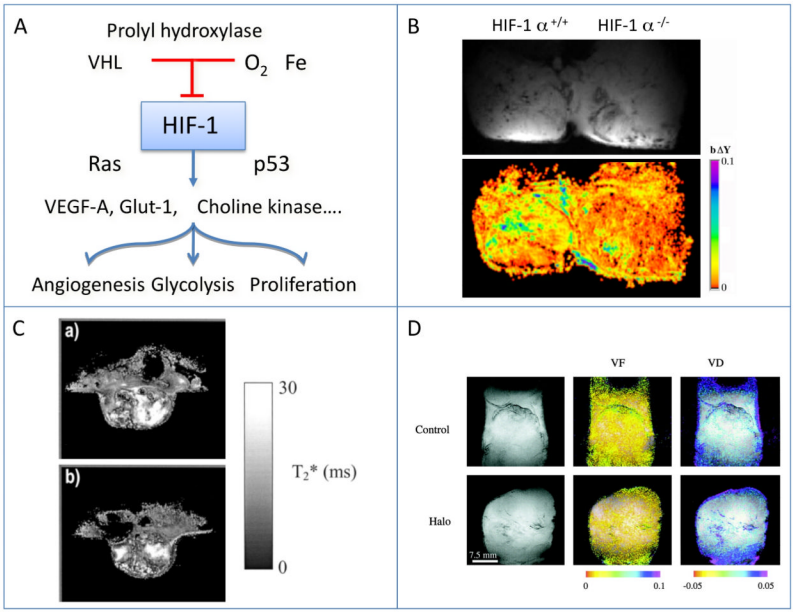

Figure 2.

HIF-1 as a regulator of cellular response to hypoxia

A) Scheme showing the hypoxic regulation of hif-1 by hypoxia, and the panel of responses induced by stabilization of hif-1alpha in hypoxic cells.

B) BOLD contrast MRI showing response to hyperoxia in Hif-1 alpha deficient ES-teratomas, from (55).

C) Hif-1 beta deficient tumors: T2* maps from a WT (a) and a c4 hif-1 beta mutant (b) tumor. Signal intensity, related to hemoglobin oxygenation, demonstrates the heterogeneity within each individual tumor rather than consistent differences between the WT and c4 tumors. Reproduced from (56).

D) VHL tumors. BOLD contrast MRI of Hippel-Lindau VHL tumors showing vascular response to hypercapnia and hyperoxia. Halo, treatment with halofuginone as antiangiogenic therapy, reproduced from (57).

Europe PMC Funders Author Manuscripts

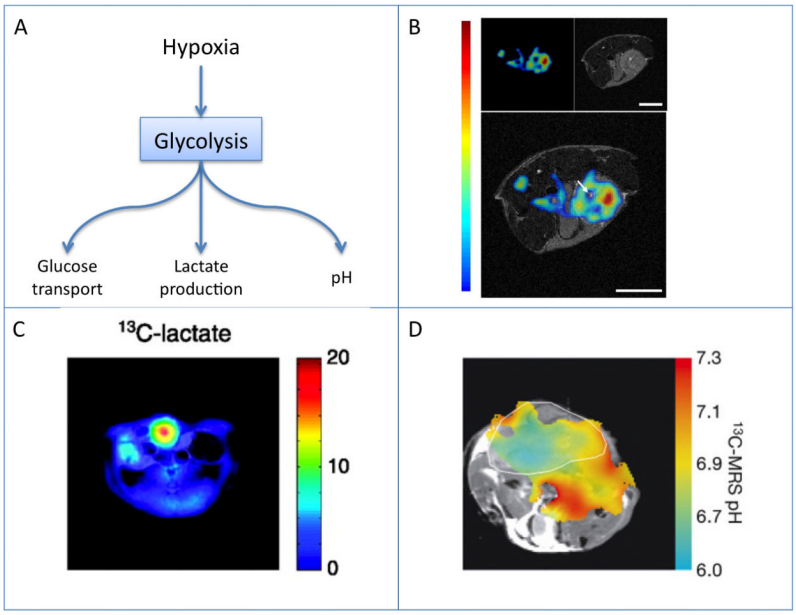

Figure 3.

Hypoxia, glycolysis, and tumor acidosis.

A) Scheme showing the role of hypoxia in mediating tumor glycolytic activity, including increased glucose uptake, lactate production and acidosis.

B) Mapping glucose uptake by simultaneous in vivo PET and MR imaging. Mouse FDG tumor imaging: (Upper Left) PET image, (Upper Right) MR image, and (Lower) fused PET and MR image. One transaxial image slice is shown. Reproduced from (65).

C) ^{13}C MRI mapping of lactate production from hyperpolarized pyruvate. Color scale maps the intensity of lactate on the anatomical 1H image. The P22 tumor tissue is indicated by the highest signal for lactate. Reproduced from (78).

D) ^{13}C MRI pH mapping of a mouse with a subcutaneously implanted EL4 tumour (outlined in white). The pH map was calculated from the ratio of the $H^{13}CO_3^-$ and $^{13}CO_2$ in ^{13}C chemical shift images acquired after intravenous injection of hyperpolarized $H^{13}CO_3^-$. Reproduced from (80).

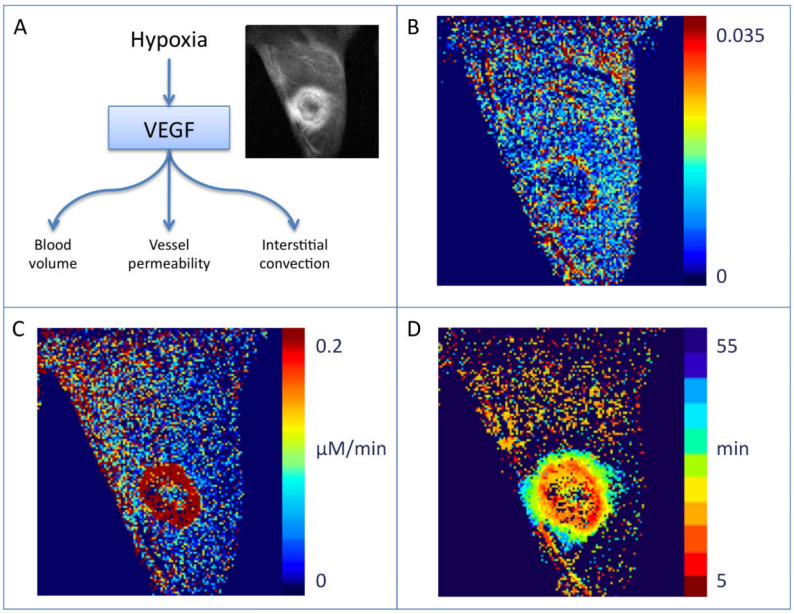

Figure 4.

VEGF as a regulator of hypoxia induced angiogenesis.

A) Scheme showing the acute effects of VEGF on vascular permeability. Sustained EGF activation leads to vascular expansion by angiogenesis. Vascular permeability induced by VEGF serves as the driving force for interstitial convection.

B-D) Analysis of DCE-MRI using biotin-BSA-GdDTPA of a VEGF over expressing C6 rat glioma tumor in a nude mouse. Reproduced from (91).

B) Blood volume fraction (fBV) maps, derived from the initial enhancement, show increased blood vessel in the tumor rim.

C) Vessel permeability, permeability surface area product (PSP) map is derived from the initial rate of accumulation of contrast media in the interstitial space.

D) Interstitial convection, Time2max map shows the gradual outward flux of contrast media from the tumor rim.

Europe PMC Funders Author Manuscripts

Europe PMC Funders Author Manuscripts

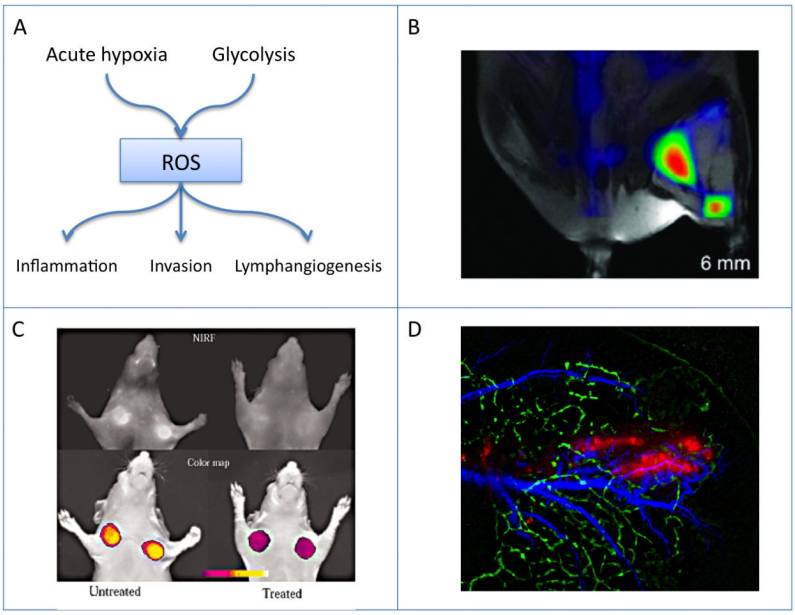

Figure 5.

Oxidative stress and metastasis.

A) Scheme showing the role of intermittent hypoxia and glycolysis in generation of reactive oxygen species (ROS). Exposure to ROS can induce inflammation, promote tumor cell invasion and stimulate lymphangiogenesis.

B) Imaging tumor inflammation, MRI-FMT of tumor associated macrophages. Reproduced from (109).

C) Imaging MMP activity. In vivo NIRF imaging of HT1080 tumor-bearing animals. Top row) raw image (700-nm emission). Untreated (left), treated with the MMP inhibitor prinomastat (right). Bottom row) color-coded tumoral maps of MMP-2 activity. Reproduced from (116).

D) Intravital imaging of peritumor lymphangiogenesis stimulated by LEDGF-induced expression of VEGF-C. C6 rat glioma tumors (red) were inoculated in the edge of cd-1 nude mouse ear. Lymphatic vessels (green) were detected by fluorescence microlymphangiography. Blood vessels (blue) were detected by dynamic light scattering imaging. Reproduced from (120).